Performance comparison of acoustic emission sensor arrays in different topologies for the localization of gas leakage on a flat-surface structure

Xiwang Cui[a,b], Yong Yan[a,c,*], Yonghui Hu[a], Miao Guo[a]
[a]School of Control and Computer Engineering, North China Electric Power University, Beijing 102206, China
[b]Key Laboratory of Noise and Vibration, Institute of Acoustics, Chinese Academy of Sciences, Beijing 100190, China
[c]School of Engineering and Digital Arts, University of Kent, Canterbury, Kent, CT2 7NT, UK

Corresponding author: y.yan@kent.ac.uk

Abstract:

The topology of the acoustic emission sensor array has an important effect on the performance of the leak localization technique. This paper compares the performances of different topologies of acoustic emission sensor arrays in the localization of gas leakage on a flat-surface structure. The principle of the leak localization is based on the near-field beamforming according to the spherical wave model and the narrowband filtering which can effectively avoid the influence of acoustic dispersion. The effect of different arrangements of the sensing elements in a sensor array on the localization accuracy is investigated and discussed. Eight typical topologies, including line, L-shaped, cross, triangle, star, circular, semi-circular and square shapes, are appraised through computer simulation. Simulation results suggest that all the arrays can perform leak localization but with different accuracies and that the L-shaped array outperforms all other topologies under the similar conditions. Furthermore, the optimal number of sensors in the L-shaped array which can maintain a reasonable accuracy of localization is analyzed. Experimental work was carried out on a laboratory scale test rig to verify and assess the effectiveness of the L-shaped array. The simulation and experimental results demonstrate that the L-shaped array is capable of identifying the location of a leak hole in a plate structure with a reasonably good accuracy.

Keywords: Gas leakage, leak localization, acoustic emission, sensor array, near-field beamforming.

Nomenclature

(a_0, b_0)	Coordinates of the leak hole	$S_i(\omega)$	Frequency spectrum of $s_i(t)$
(a_i, b_i)	Coordinates of the sensors	$S_{ref1}(t)$	Signal of the reference sensor corresponding to the leak hole
(a_s, b_s)	Coordinates of the scanning point	$S_{ref1}(\omega)$	Frequency spectrum of $s_{ref1}(t)$
c	Speed of the acoustic wave	$S_{ref2}(t)$	Signal of the reference sensor corresponding to the scanning point
d_i	Distance between the leak hole and the sensor i	$S_{ref2}(\omega)$	Frequency spectrum of $s_{ref2}(t)$

D_i	Distance between the scanning point and the sensor *i*	$W_1(\omega)$	Weighting vector corresponding to the leak hole
E_p	Energy of the sensor array at scanning point P	$W_2(\omega)$	Weighting vector corresponding to the scanning point
L	Equivalent length of sensor array	X(ω)	Frequency spectral matrix corresponding to leak hole
r	Distance between the leak hole and the sensor array	Y(ω)	Frequency spectral matrix corresponding to the scanning point
$s_i(t)$	Signal received by sensor *i*	λ	Wavelength of the leak signal
		τ_i	Time delay

1. Introduction

Flat-surface structures are ubiquitous in gas transportation and storage facilities such as power plants with Carbon Capture and Storage (CCS) capability or Liquefied Natural Gas (LNG) [1]. Adequate assessments and preventive measures must be taken into consideration to minimize risks of potential leakages from such facilities. Therefore, rapid leak localization techniques are essential for the safe transportation and storage of high-pressure gaseous or liquid materials. Several methods have been proposed for leak detection and localization, including those based on tracer tracking, electromagnetic scanning, optical fiber sensing, infrared thermography, acoustic emission (AE) detection and mass balancing (flow equilibrium) [2-5]. Amongst these methods, AE detection is regarded as promising because of its low cost, small size, simple structure, high sensitivity and easy installation [6].

When a leak occurs on a flat-surface structures, the leak hole will generate acoustic waves. An AE sensor array serves to detect the acoustic waves and inform the localization algorithm to localize the leakage. In recent years, several leak localization techniques have been studied. These include the time difference of arrival (TDOA) technique based on basic cross correlation and generalized cross correlation [7], the array signal processing technique based on beamforming and spatial spectrum estimation [8], and the artificial intelligence technique based on neural networks, genetic algorithms or deep learning [9-12]. The TDOA technique is widely used for leak localization on pipelines for several decades, however, its localization accuracy depends significantly on the degree of signal correlation [13]. Poor signal similarity and hence false or wide peaks of the cross-correlation function in some cases make the TDOA results unreliable. Wilcox *et al*. [14] studied the propagation and dispersion effect of an acoustic wave in the metal structure and their results demonstrated that the shape of the wave-packet became blurred and distorted with the increase of the propagation distance. This result indirectly explains the reason why the cross-correlation technique is not accurate in calculating the TDOA of the AE signals. In order to eliminate the influence of signal dispersion and distortion, many researchers attempted some signal decomposition and reconstruction algorithms prior to the leak localization process, such as wavelet transform, empirical mode decomposition and time reversal [15-18]. These algorithms have improved, to some extent, the localization accuracy, but have greatly increased the complexity and computation time of the signal processing. The emerging

artificial intelligence technique by combining feature extraction with neural network training can achieve accurate localization results in theory. However, the requirement for a high volume of training data and computation time makes it impractical for on-line real-time applications. Furthermore, the shape and size of the leak holes vary from one case to another, so the acoustic signals generated from the different holes are different [19]. Therefore, it is challenging to accurately predict the location of leakage holes using the existing artificial intelligence technique with limited datasets.

Beamforming is an array signal processing technique through delaying, summing and other weighting algorithms, which is widely used in the communication, radar and sonar fields [20]. In this technique the gain in the desired direction is increased and the unwanted information such as interference and noise is suppressed. Thus, this technique can enhance target localization, signal enhancement and interference suppression. In comparison with the TDOA and artificial intelligence techniques, the beamforming approach can improve the leak localization accuracy by integrating signal characteristics from multiple sensors and does not need complex and time-consuming computing algorithms. Array topology is a key factor to consider the leak localization performance because different array arrangements have different spatial resolutions and directivities. Some researchers focused on a certain array arrangement to study its applicability and localization accuracy, such as a line array proposed by Yan *et al*. [21], an L-shaped array proposed by Bian *et al*. [22], a circular array proposed by Cui *et al*. [23], and a sparse irregular array proposed by Niri *et al*. [24]. However, there is lack of a systematic performance comparison of AE sensor arrays in different topologies for the localization of gas leakage.

This paper attempts for the first time to compare systemically the topologies of AE sensor arrays and assess their performances for the localization of gas leakage on a flat-surface structure. The near-field beamforming technique combined with a spherical wave propagation model and narrowband filtering is proposed to achieve the localization of the leak hole on a metal plate.

2. Topology of a sensor array

A number of sensors are commonly combined to form an array in practical applications in order to acquire information from the target being detected and achieve data fusion. The topology of a sensor array is the spatial geometrical layout of the sensing elements. It is well known that, for a large area of leak detection, the resolution and accuracy of a localization technique will increase with the number of sensors. However, a large number of sensors usually entail high capital cost of the localization system, high computational requirement and poor real-time response. It is a challenge to use a less number of sensors to achieve a localization result as accurate as possible. In this study, the significance of the topology of the sensor array on the performance and the number of sensors used in the localization system are studied. Eight typical candidate topologies, including line, L-shaped, cross, triangle, star, circular, semi-circular and square arrangements, are compared and analyzed.

2.1 Line array

A line array, as shown in Fig. 1, is the most common layout in practical applications and is also a fundamental element to constitute more complex arrays. This sensor array has obvious advantages such as simple structure, convenient installation and easy sensor coordinate definitions. Usually the line array is arranged with the sensors evenly distributed and the spacing between the adjacent sensors is a key parameter of the line array. This sensor layout is most sensitive to information from the direction perpendicular to the line axis.

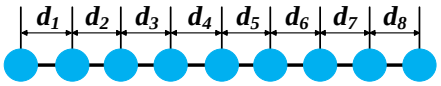

Fig. 1. Sensor layout of a line array

2.2. L-shaped array

This array can be seen as two line arrays arranged in an L-shape as shown in Fig. 2. The L-shaped array can take into account the information from both horizontal and vertical axes concurrently in addition to all other advantages of the line array.

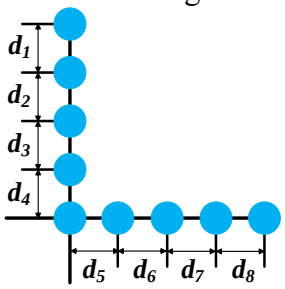

Fig. 2. Sensor layout of an L-shaped array

2.3 Cross array

A cross array comprises two line arrays arranged perpendicular to each other, as shown in Fig. 3. The cross array appears similar to the L-shaped array to some extent, but it can be regarded as two L-shaped arrays opposite to each other with a shared corner. The spacing between any adjacent sensors is not necessarily a constant.

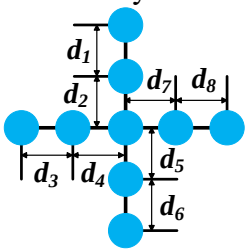

Fig. 3. Sensor layout of a cross array

2.4 Triangle array

A triangle array consists of three line arrays in the form of a triangle. Fig. 4 shows such an array with an equal number of sensors in each side of the triangle. The key parameters of this type of array are the angle between the adjacent line arrays and the spacing between the adjacent sensors.

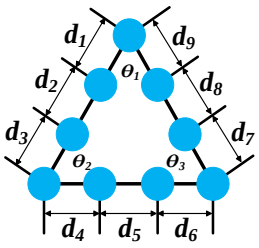

Fig. 4. Sensor layout of a triangle array

2.5 Star array

A star array is also formed by three line arrays like the triangle array, but in an open type of topology. Fig. 5 shows a star array with three sensors in each of the line arrays.

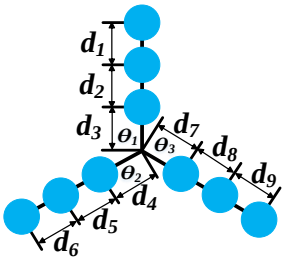

Fig. 5. Sensor layout of a star array

2.6 Circular array

Sensors in this array are arranged in a circle with a diameter of D (Fig. 6). The appearance of the circular array appears regular, but the coordinate definitions of each sensor can be more complex than that in other arrays. The key parameters of this array are the angle between the adjacent sensors and the diameter of the circle. According to the angle between the adjacent sensors, a circular array can be regarded as a uniform array and a non-uniform array.

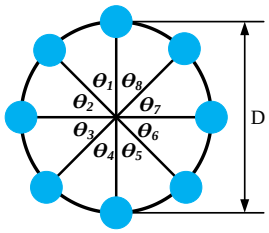

Fig. 6. Sensor layout of a circular array

2.7 Semi-Circular array

A semi-circular array is shown in Fig. 7. If the same number of sensors is used, the spacing between the adjacent sensors is half of that in the circular array. The key parameters of this array are same as the circular array, including the angle between the adjacent sensors and the diameter of the circle.

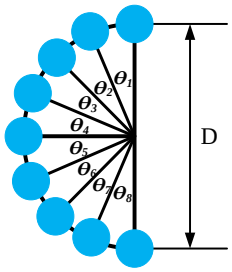

Fig. 7. Sensor layout of a semi-circular array

2.8 Square array

A square array is formed by four linear arrays. Fig. 8 shows an example of this with eight sensors. This topology takes slightly more space in area than the circular one for the same number of sensors, assuming the side of the square equals to the diameter of the circle. The square array can be regarded as two L-shaped arrays arranged in an enclosed form.

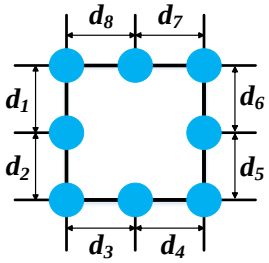

Fig. 8. Sensor layout of a square array

It must be stressed that, in this study, the sensors in each of the eight candidate topologies are evenly distributed in terms of physical spacing. Such even sensor arrays are more readily manufactured and easier to install than uneven arrays in practical applications. Uneven arrays can have many different topological combinations for the same number of sensors. A detailed comparative study of uneven arrays with reference to the even arrays is beyond the scope of this paper.

3. Principles of the leak localization

A beamforming leak localization technique can be classified as near-field model or far-field model [25], according to the distance between the leak hole and the sensor array. According to the empirical formula, the case can be regarded as a near-field model when the following equation is satisfied,

$$r \leq \frac{2L^2}{\lambda} \tag{1}$$

where r is the distance between the leak hole and the sensor array, L is the equivalent length of the sensor array, and λ is the wavelength of the leak signal at a particular frequency. Meanwhile, the case is considered as a far-field model, if the following equation is met,

$$r > \frac{2L^2}{\lambda} \tag{2}$$

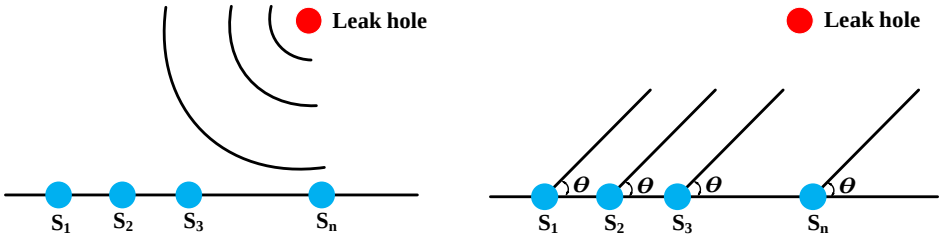

(a) Near-field model (b) Far-field model

Fig. 9. Models of the beamforming technique

In the near-field model the wave front curvature of the acoustic wave generated from the leak hole is simplified as a spherical wave, as shown in Fig. 9(a), so the signal from a sensor is a function of the angle between the spherical wave and the sensor and the distance from the leak hole to the sensor. Thus, one array is sufficient to locate the leak hole. In the far-field model, however, the wave front curvature of the signal can be ignored and hence be regarded as a planar wave (Fig. 9(b)). The far-field model can only provide the directional information about the leak hole, so at least two arrays are thus required to locate the leak hole through the intersection of two different directions. In comparison to the far-field model,

the near-field model requires a fewer number of sensors from this point of view. In the near-field model, the size and topology of the array are not negligible relative to the distance between the leak hole and the sensor array. Fig. 10 shows the near-field model of the leak localization with a line array.

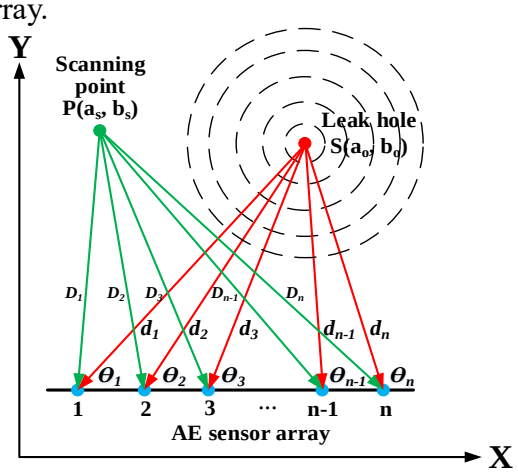

Fig. 10. Near-field model of leak localization with a linear array

Suppose a fundamental linear sensor array consisting of n sensors is arranged in the near-field model and the coordinates of the sensor i are (a_i, b_i), i=1, 2, … , n. If the coordinates of the leak hole are (a_0, b_0), then the distance (d_i) between the leak hole and sensor i is given by

$$d_i = \sqrt{(a_i - a_0)^2 + (b_i - b_0)^2} \tag{3}$$

Taking sensor 1 as the reference sensor, we can determine the time delay (τ_i) between the acoustic waves from sensor 1 and sensor i:

$$\tau_i = \frac{d_i - d_1}{c} \tag{4}$$

where c is the speed of the acoustic wave.

Suppose $S_{ref1}(t)$ is the signal received by the reference sensor, then the signal received by sensor i, $s_i(t)$, can be regarded as a time-delayed version of $S_{ref1}(t)$:

$$s_i(t) = s_{ref1}(t - \tau_i) \tag{5}$$

The frequency spectrum of $s_i(t)$ is given by

$$\begin{aligned} S_i(\omega) &= \int_{-\infty}^{+\infty} s_i(t) e^{-j\omega t} dt = \int_{-\infty}^{+\infty} s_{ref1}(t - \tau_i) e^{-j\omega t} dt \\ &= S_{ref1}(\omega) e^{-j\omega\tau_i} \end{aligned} \tag{6}$$

where $S_i(\omega)$ and $S_{ref1}(\omega)$ are the frequency spectra of $s_i(t)$ and $S_{ref1}(t)$, respectively, and ω is the angular frequency. Equation (6) indicates that, under the assumption of narrow band signals, the time delay can be approximated as a phase shift. The signals received by the sensor array can thus be expressed as:

$$X(\omega) = [S_1(\omega), S_2(\omega), \ldots, S_n(\omega)]^{\mathrm{T}} = W_1(\omega) S_{ref1}(\omega) \tag{7}$$

where $W_1(\omega)$ is a weighting vector:

$$W_1(\omega) = [1, e^{-j\omega\frac{d_2 - d_1}{c}}, \ldots, e^{-j\omega\frac{d_n - d_1}{c}}]^T \tag{8}$$

In practice, the coordinates of the leak hole are unknown in advance and need to be identified. The principle of the near-field beamforming is to scan the whole detection area and find the leak hole. Assume a point P (a_s, b_s) is an arbitrary scanning point in the flat-surface structure as shown in Fig. 10, then the distance between this point and the sensor i is calculated from:

$$D_i = \sqrt{(a_i - a_s)^2 + (b_i - b_s)^2} \tag{9}$$

Suppose $S_{ref2}(t)$ is the signal received by the reference sensor in the scanning condition, $S_{ref2}(\omega)$ is the frequency spectra of $S_{ref2}(t)$, then the signals received by the sensor array in the frequency domain are expressed as:

$$Y(\omega) = W_2(\omega) S_{ref\,2}(\omega) \tag{10}$$

where $W_2(\omega)$ is a new weighting vector:

$$W_2(\omega) = [1, e^{-j\omega\frac{D_2 - D_1}{c}}, \ldots, e^{-j\omega\frac{D_n - D_1}{c}}]^T \tag{11}$$

Therefore, the output energy of the sensor array at the scanning point P is given by:

$$E_p = E[X(\omega)Y^T(\omega)] = W_1(\omega)E[S_{ref\,1}(\omega)S_{ref\,2}(\omega)]W_2(\omega)^T \tag{12}$$

where $E[\cdot]$ denotes the expectation.

By scanning all the points in the detection area and calculating the corresponding output energy of the sensor array, an energy distribution profile of the whole scanning field can be drawn. When the scanning point and the actual leak hole happen to overlap at the same position, the output energy of the sensor array would be maximum because the $X(\omega)$ and $Y(\omega)$ have the same phase. In this case there will be a peak in the energy distribution profile.

4. Simulation studies

Physical experiments are often time consuming, costly and have inevitable uncertainties. It is also hard to identify subtle differences between arrays with similar topologies. Thus, in order to appraise and compare the localization performance of different sensor topologies, the eight typical candidate arrays are studied through computer simulation.

4.1 Simulation considerations

In the simulation study the number of sensors, distance between adjacent sensors, equivalent size and center location of each array are set the same or similar as much as possible. In general, the number of sensors should not be too many in order to control cost of the system. Meanwhile, it should be bore in mind that the least number of sensors to form different array topologies are different. For instance, at least three sensors are required in the L-shaped array and more than four sensors are required in the square and circular arrays. In addition, an odd number of sensors is better to maintain the symmetrical topologies for the L-shaped, cross and semi-circular arrays while an even number of sensors is better to maintain a uniform topology for the circular and square arrays. In the simulation study, nine sensors are used to make most of the candidate topologies, whereas, for the circular and square arrays, the number of sensors is restricted to eight.

Simulation was carried out using a set of bespoke codes within MATLAB (version R2016a). Fig. 11 illustrates the key steps in the simulation procedure. The area of the scanning field in the simulation is set to 100 cm × 100 cm and scanning step (mesh size) is 1 cm both in X and Y directions. There are a total of 10,000 scanning points with a resolution of 1 cm^2. In the simulation study the leak hole is assumed to be in the center of the flat-surface structure and its coordinates are (50 cm, 50 cm). The equivalent size and installation positions of the typical candidate arrays are shown in Fig. 12. In order to reduce the influence of echoes, the sensor arrays should not be too close to the boundaries of the flat-surface structure in practice, thus the distance between the sensor and the boundary is greater than 5 cm. The frequency of the leak signal is set to 160 kHz, which is the main frequency of the actual leak signal as measured using the AE sensors (Section V) with a SNR (signal-to-noise ratio) of 10 dB. In practice, however, a leak signal may consist of a range of frequencies as well as significant dispersion, i.e., different frequency components have different wave speeds. For this reason, a narrow-band filter is usually used to process

the wide-band leak signal to control the frequency band of the signal (ideally a single frequency component) and hence improved localization performance. If we assume the frequency components in the narrow-band signal travel at the same wave speed, then each frequency component in the signal will generate the same weighting vector and hence the same energy distribution profile. It is because a single-frequency signal is equivalent to a narrow-band signal under the given conditions that it is used in this simulation study.

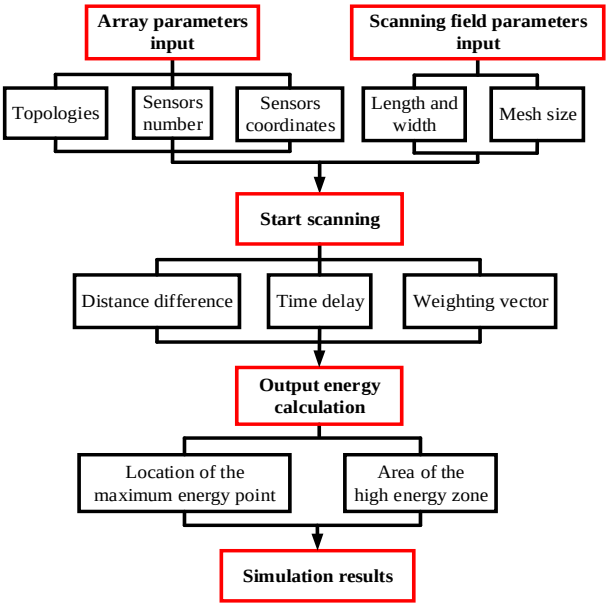

Fig. 11. Flowchart of the simulation

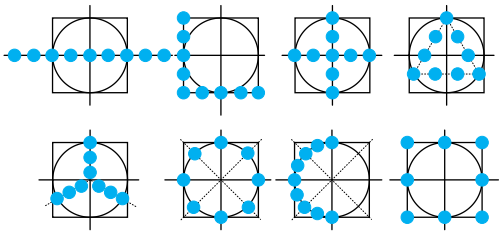

(a) Equivalent size of the typical candidate arrays

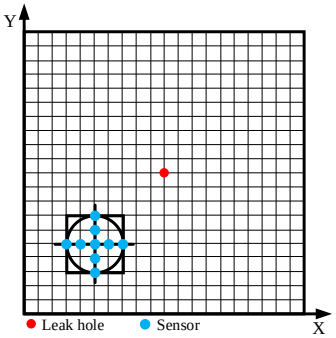

(b) Equivalent positions of the typical candidate arrays

Fig. 12. Equivalent size and positions of the typical candidate arrays

4.2 Simulation results

4.2.1 Line array

Fig. 13 shows the 2D and 3D energy distributions using the linear array. The white irregular shape in the centre indicates a high energy zone. The red asterisk '*' in Fig. 13(a) marks the point with the maximum energy whilst 'o' indicates the location of the sensor

array. The energy scale is normalized to the range between 0 and 1.

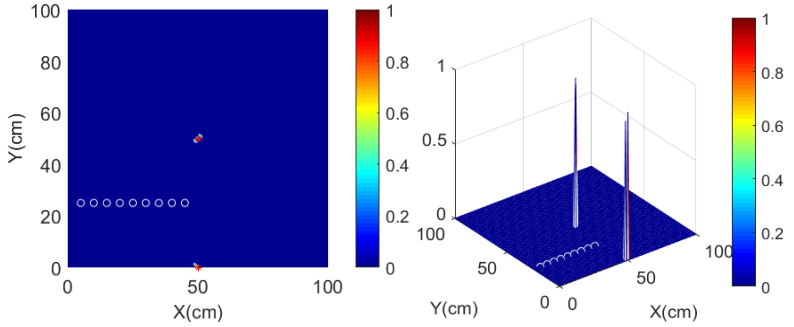

(a) 2D Results (b) 3D Results

Fig. 13. Localization results of the linear array

It can be seen from Fig. 13 that the simulation results indicate that, in principle, there are two high energy zones in the flat-surface structure. One of these is located at (50 cm, 50 cm), where the leak hole is located, whereas the other one of the maximum energy points is located at (50 cm, 0 cm). Since the vertical coordinate of the line array is 25 cm, it can be seen that these two maximum energy points are symmetric about the line array. The reason for this phenomenon is that the line array is a one-dimensional topology. If two leak holes are symmetric about the array, the distance and phase shift from these two leak holes to the array are the same. Thus the energy distributions on both sides of the line array are symmetric, where the sensor array acts like a mirror.

4.2.2 L-shaped array

Fig. 14 shows that there is a clear high energy zone in the center of the detection area and the location of the maximum energy is indeed at the leak hole. The L-shaped array performs very well in the simulated localization in this case.

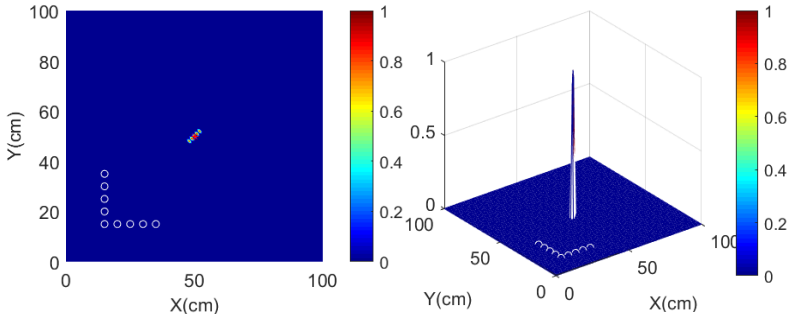

(a) 2D Results (b) 3D Results

Fig. 14. Localization results of the L-shaped array

4.2.3 Cross array

Fig. 15(a) and (b) show that there is a long and narrow high energy zone in the center of the detection area. The location of the maximum energy is the same as the leak hole, however, the area of this high energy zone is much greater than that of the line and L-shaped arrays. This is because the leak hole is at the upper-right of the array, so the sensors in the upper-right of the array play the dominant role and other sensors in the bottom-left of the array are “blocked” by those on the upper-right. In order to study this phenomenon, the sensors on the top and left are removed respectively, and the results are plotted in Fig. 15(c) and (d). It can be seen that the localization performance deteriorates when the top sensor in the cross array is removed (Fig. 15(c)) while the localization performance has almost no change when the left sensor in the cross array is removed (Fig. 15(d)).

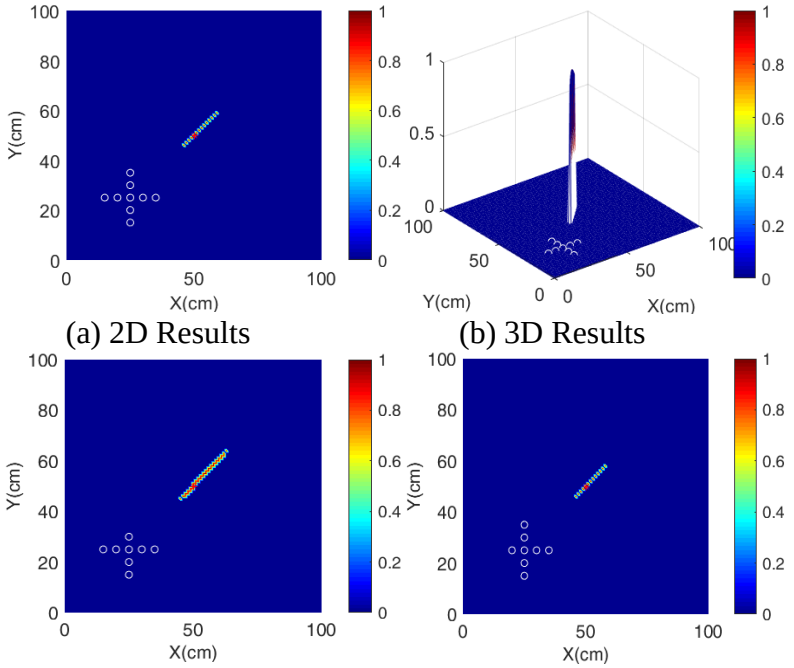

(a) 2D Results (b) 3D Results

(c) 2D Results without the top sensor (d) 2D Results without the left sensor

Fig. 15. Localization results of the cross array

4.2.4 Triangle array

Fig. 16(a) and (b) show that there is a long and narrow high energy zone in the center of the detection area just like the cross array and the location of the maximum energy is the same as the leak hole. The primary sensors in the triangle array are also the upper-right ones. Again, this is confirmed by removing the top and left sensors, respectively, as shown in Fig. 16 (c) and (d).

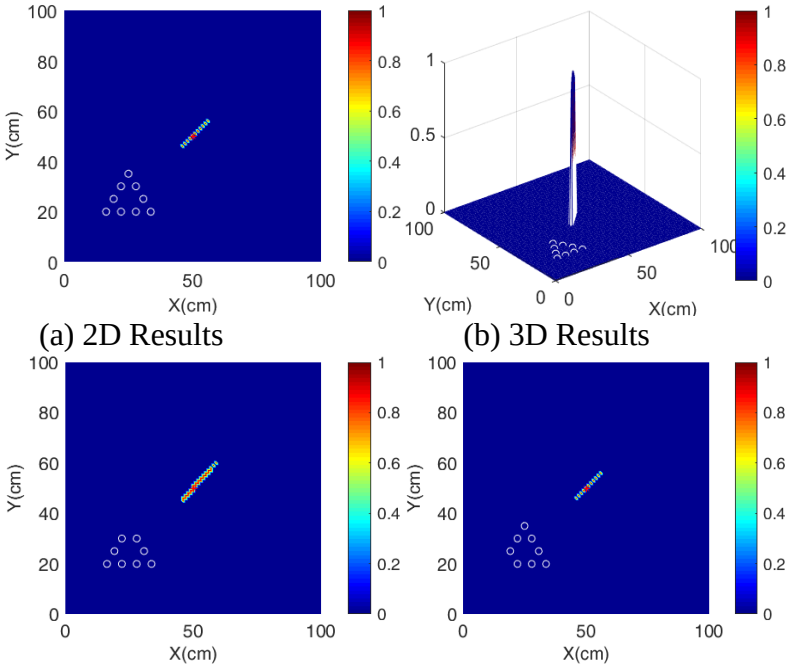

(a) 2D Results (b) 3D Results

(c) 2D Results without the top sensor (d) 2D Results without the left sensor

Fig. 16. Localization results of the triangular array

4.2.5 Star array

It can be seen from Fig. 17 that there is a long high energy zone in the center of the

detection area just like the cross and triangle arrays, but this high energy zone is a little wider than that of the cross and triangular arrays. The results illustrate that the cross, triangle and star arrays have a similar localization performance because of their similar topologies. The slight differences between them in performance are due to the positions of the primary sensors.

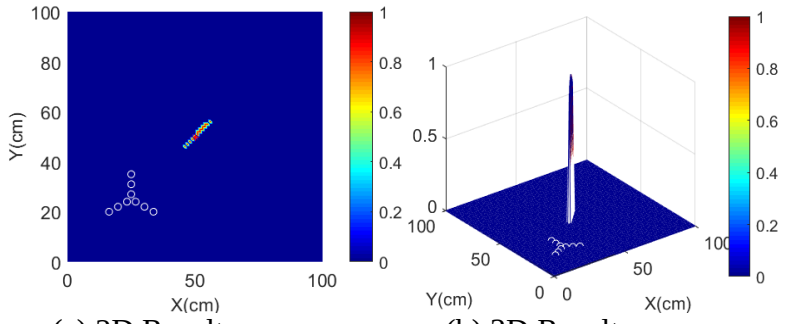

(a) 2D Results (b) 3D Results

Fig. 17. Localization results of the star array

4.2.6 Circular array

Fig. 18 shows that there is a clear high energy zone in the center of the flat-surface structure and the maximum energy point is also the same as the leak hole. The circular array outperforms the cross, triangle and star arrays because all the sensors in the circular array distribute on the perimeter of the circle and this decentralized topology avoids blocking other sensors to some extent.

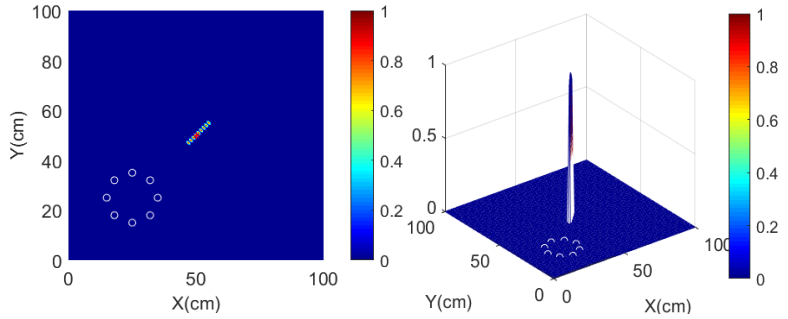

(a) 2D Results (b) 3D Results

Fig. 18. Localization results of the circular array

4.2.7 Semi-circular array

It can be seen from Fig. 19 that there is a clear high energy zone in the center of the flat-surface structure and the maximum energy point is also the same as the leak hole. The localization results of the semi-circular array are similar as that of the circular array because of their similar topologies. However, the area of the narrow high energy zone of the semi-circular array is a slightly greater than that of the circular array. This is because the sensors in the semi-circular array are concentrated on a half perimeter of the circle and the spacing between the adjacent sensors is small. In addition, the localization functions of adjacent sensors will overlap to some extent. In this sense, the array with properly decentralized topology can acquire more information and hence achieve better results in the near-field model.

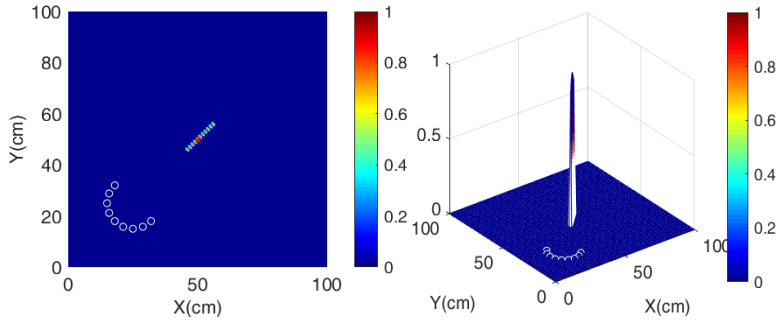

(a) 2D Results (b) 3D Results

Fig. 19. Localization results of the semi-circular array

4.2.8 Square array

It can be seen from Fig. 20 that there is a clear high energy zone in the center of the detection area and the maximum energy are located at the leak hole. Just like the circular array, the square array has a similar decentralized topology and hence good localization performance.

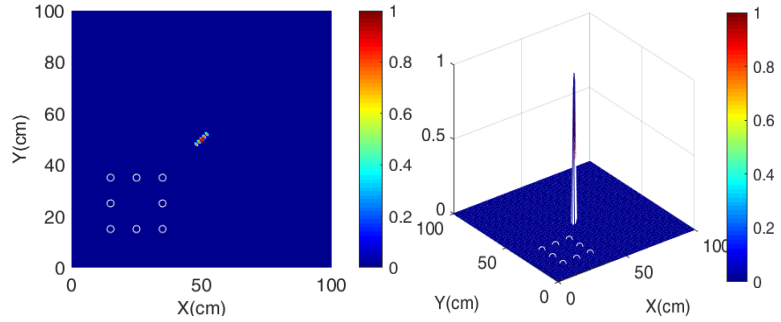

(a) 2D Results (b) 3D Results

Fig. 20. Localization results of the square array

4.3 Comparison and analysis

Fig. 13-20 indicate that each candidate array can find the leak hole in the obtained high energy zone. However, since the energy value of every point in the high energy zone is actually very close to each other, it can be concluded that the localization accuracy is better if the area of the high energy zone is smaller. TABLE I shows the area of the high energy zone of each candidate array.

Table 1
Area of the high energy zone of each candidate array

Shape	Area (cm^2)
Line	5
L-shaped	5
Cross	15
Triangle	11
Star	15
Circular	9
Semi-Circular	11
Square	5

It can be seen from Table 1 that the line, L-shaped and square arrays have the best localization performance. The circular, semi-circular and triangle arrays also perform well. The cross and star arrays are the worst in terms of localization performance.

Although the line array is one of the best topologies, the existence of the pseudo leak hole affects the localization result and additional methods are required to identify which one is the true leak hole in practical application. Therefore, it is worthwhile to further compare the localization performances of the L-shaped and square arrays to find the optimal topology. The above simulation results are based on the condition that the equivalent size of each array stays the same or similar as much as possible. Fig. 12(a) shows that the equivalent size of the L-shaped and square arrays are the same, however, their distances between adjacent sensors are different. The distance between adjacent sensors of the L-shaped and square-shaped arrays are 5 cm and 10 cm, respectively.

According to the above simulation results, the decentralized topologies have good localization performance. Thus, the distance between adjacent sensors of the L-shaped array is increased to 10 cm, the same as the square array. The localization results are shown in Fig. 21. It can be seen from Fig. 21 that there is a clear high energy zone in the center of the flat-surface structure and the area of this high energy zone is only 1 cm^2. Therefore, the L-shaped array outperforms the square array (5 cm^2) in such circumstances.

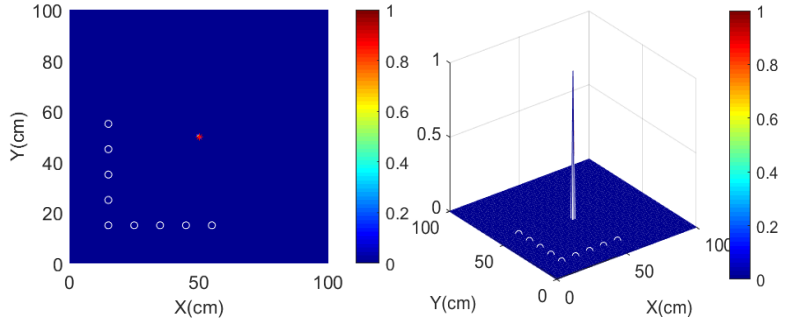

(a) 2D Results (b) 3D Results

Fig. 21. Localization results of the L-shaped array (distance between adjacent sensors is 10 cm)

In the premise of keeping a reasonable accuracy of the localization result, the least number of sensors in the L-shaped array is further studied and simulated in order to reduce the computational cost for practical application. Fig. 22 shows the localization results by using 8, 7, 6, 5 and 4 sensors in the array, respectively. Table 2 shows the area of the high energy zone with different number of sensors.

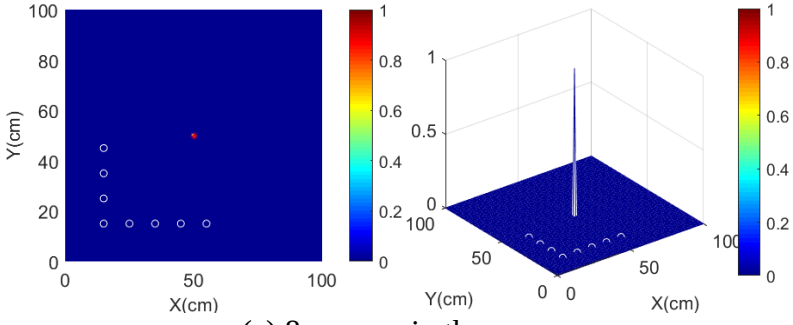

(a) 8 sensors in the array

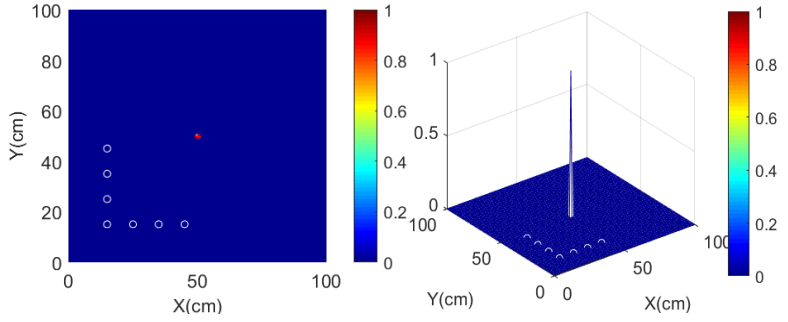

(b) 7 sensors in the array

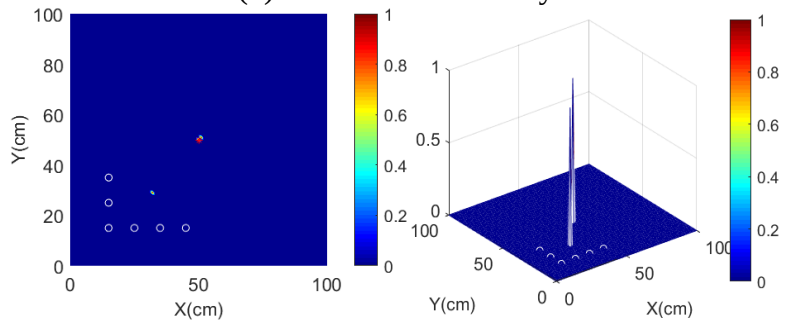

(c) 6 sensors in the array

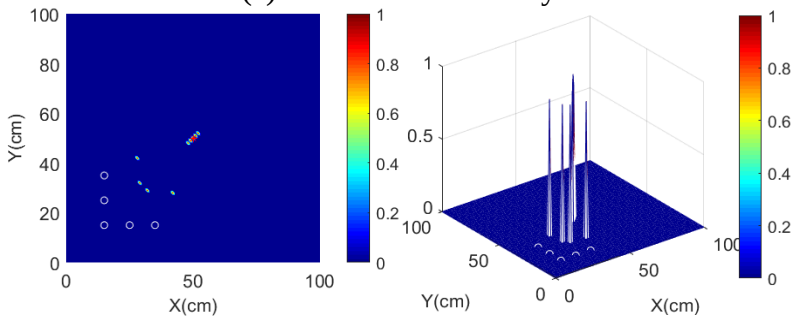

(d) 5 sensors in the array

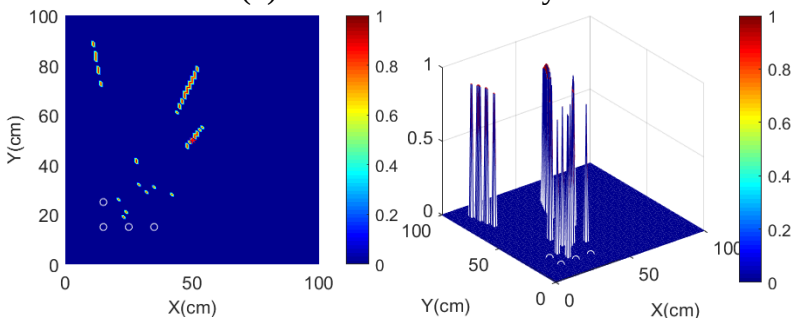

(e) 4 sensors in the array

Fig. 22. Localization results by using different number of sensors

Table 2
Area of the high energy zone with different number of sensors

Number of Sensors	Area (cm^2)
9	1
8	1
7	1
6	3
5	9
4	52

It can be seen from Fig. 22 and Table 2 that the localization performance deteriorates with the reduction in the number of sensors, especially when it is less than five. In this study the optimal number of sensors in the L-shaped array is seven. The optimal number of sensors depends on practical applications. This study demonstrates that computational simulation provides a cost-effective approach to identifying the optimal number of sensors for a given application.

5. Experimental results and discussion

5.1 Experimental set-up

In order to verify and assess the effectiveness of the L-shaped array, an experimental set-up was built in the laboratory environment. Experiments were carried out on a 304 stainless plate with dimensions of 100 cm × 100 cm × 0.4 cm. A simulated CO_2 leakage was created at a pressure of 1 bar from a hole with 1 mm diameter in the center of the plate. An L-shaped array with 7 AE sensors was evenly mounted on the plate using vacuum grease couplant. Leakage signals were pre-amplified using AE amplifiers with a bandwidth of 10 kHz - 1 MHz at 40 dB amplification to reduce the influence of noises and interferences. A 7-channel holographic AE signal recorder (Model type DS2-8A, Softland Co. Ltd) was used for waveform acquisition at a sampling rate of 3 MHz. The sensor arrangement and experimental set-up are shown in Fig. 23. The main technical specifications of the AE sensor (Model type RS-2A, Softland Co. Ltd) are shown in Table 3 and the frequency response characteristics of the AE sensor are plotted in Fig. 24. The frequency band of the AE sensors used in this study is very wide (50 kHz - 400 kHz) in order to acquire as much information as possible about the leak. Narrow band sensors should be selected in practical applications in order to reduce hardware cost.

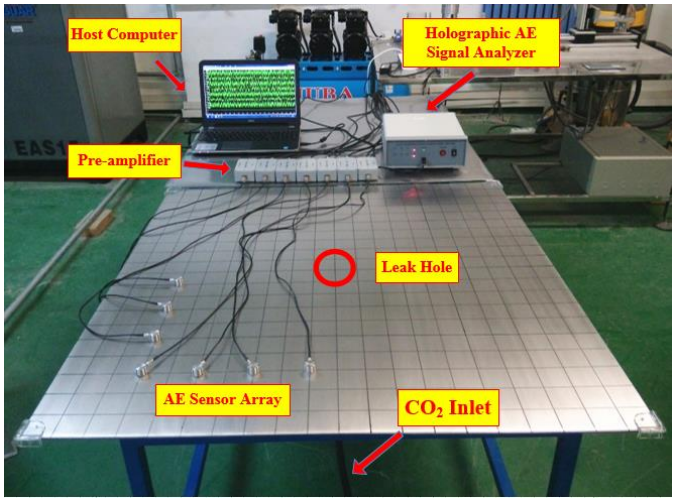

Fig. 23. Sensor array arrangement and experimental set-up

Table 3
Technical specifications of the AE sensor

Property	Value
Diameter	18.8 mm
Height	15 mm
Operating frequency range	50 kHz - 400 kHz
Operating temperature	-20 °C - 200 °C

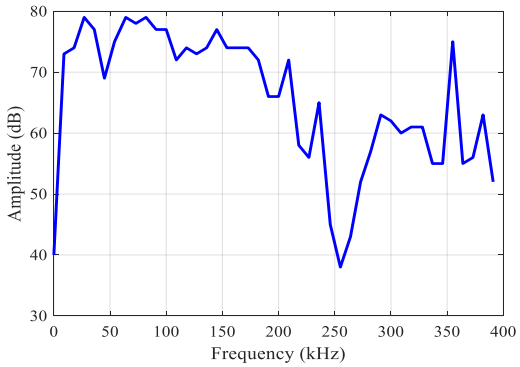

Fig. 24. Frequency response of the AE sensor

5.2 Signal characteristics

The time domain waveform and corresponding power spectral density (PSD) of the leakage signal received by the AE sensor are plotted in Fig. 25. Fig. 25(a) indicates that the leakage signal generated from a 1 mm hole is weak and its peak amplitude is nearly 20 mv, meanwhile the noise of the measurement system is also very low with a maximal amplitude no greater than 3 mV. Fig. 25(b) shows that the leak signal has a wide spectral range from 20 kHz to 300 kHz. The signal contains frequency components in two main regions, one in the high frequency band (150 kHz - 170 kHz), the other in the low frequency band (30 kHz - 70 kHz). Since the high frequency region is not adversely affected by the ambient noise such as the compressor, the signal in this region is utilized for the localization of the leak hole in this study.

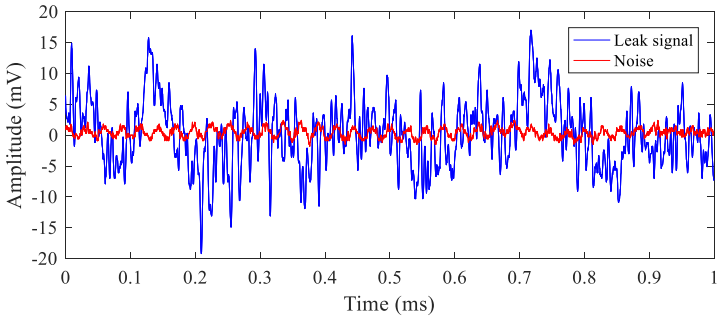

(a) Time domain

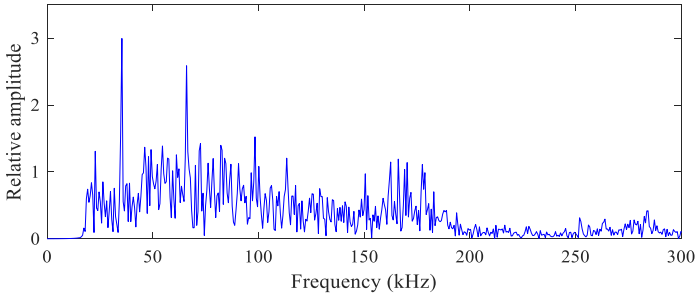

(b) Frequency domain

Fig. 25. Time domain signal waveform from sensor 1 and the corresponding PSD

5.3 Results and discussion

Given that AE wave has different speed and mode with different frequencies [26], a narrow band signal is extracted in order to eliminate the effects of speed changes and achieve accurate localization results. Thus, an FIR (finite impulse response) narrow-band digital filter is deployed in view of its advantages such as linear phase, high precision and flexibility in configuring the filter characteristics. The narrow band FIR filter was designed using MATLAB Filter Design and Analysis Tool. The frequency band of the filter is [157 kHz, 163 kHz], thus the central frequency is 160 kHz and bandwidth is 8 kHz. The advantages of high-frequency narrow-band signals include high spatial resolution, steady wave speed, and immunity from contamination by low-frequency mechanical noise. The mean speed of the acoustic wave near the frequency of 160 kHz is 4000 m/s which was measured by combining the Nielsen-Hsu Pencil Lead Break Test. Fig. 26 shows the PSD of the leak signal after filtering and Fig. 27 indicates the experimental localization results.

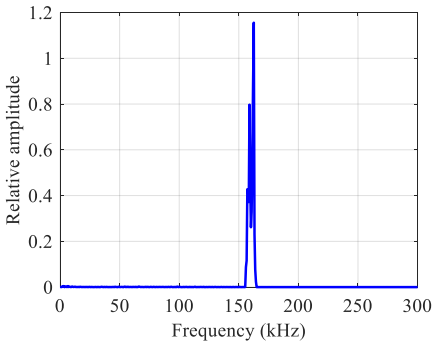

Fig. 26. PSD of the leak signal after narrow-band filter

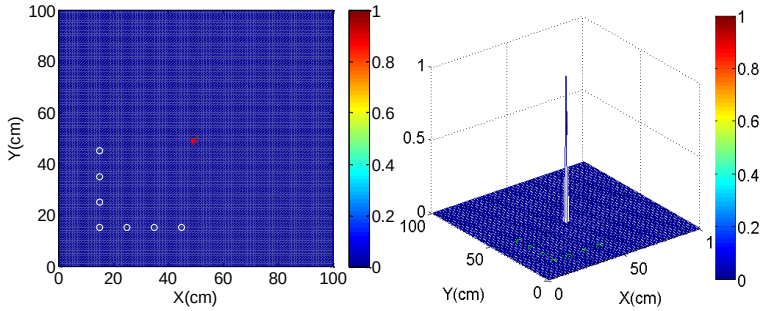

(a) 2D Results (b) 3D Results

Fig. 27. Experimental localization results

It can be seen from Fig. 27 that there is a clear high energy zone in the center of the flat-surface structure like the corresponding simulation results. However, there is a little difference between the simulation and the experimental results in that the area of the high energy zone in the simulation result is only 1 cm^2, while the area in the experimental result is 2 cm^2, which can be seen more clearly in the zoomed-in version (Fig. 28). This is because that the experimental signal includes noise, reflection and distortion which is more complex than the simulation. Table 4 shows the coordinates and corresponding energy value of the localization points in the 2 cm^2 high energy zone.

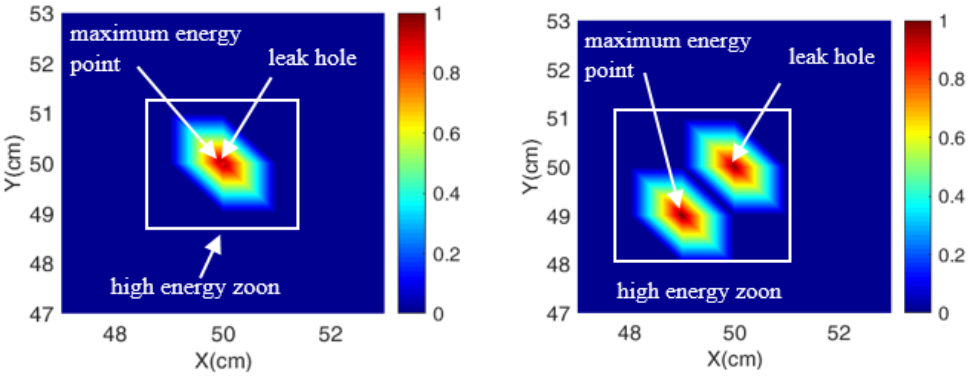

(a) Simulation result (b)Experimental result

Fig. 28. Zoomed-in version of Fig. 27

It can be seen from Table 4 that the coordinates and energy of these two localization points are very close. Given that the coordinates of the actual leak hole are (50 cm, 50 cm), the absolute error in the dimensional measurement on the flat-surface (i.e. the absolute distance between the measured location and expected location of the leak hole) is $\sqrt{2}$ cm, which is equivalent to a full-scale error of 1.4% (The full-scale error is defined as the absolute error normalized to the full length of the square plate). In summary, this result indicates that the L-shaped array is capable of providing accurate localization of gas leakage on a flat-surface structure in the experiment.

Table 4
Localization results

Coordinates	Energy
(49 cm, 49 cm)	1.0000
(50 cm, 50 cm)	0.9873

6. Conclusions

The influence of the topologies of the AE sensor arrays on the localization performance of gas leakage on a flat-surface structure has been studied. The geometrical characteristics, advantages and shortcomings of eight typical topologies including the line, L-shaped, cross, triangle, star, circular, semi-circular and square shapes have been analyzed, compared and simulated. Simulation results have suggested that all these arrays can perform leak localization but with different accuracies and that the L-shaped array outperforms all other topologies under the similar conditions. Moreover, an array with a properly decentralized topology can acquire more information and achieve better localization performance in the near-field model. The localization performance will deteriorate with reducing number of primary sensors in the array. The optimal number of sensors in the L-shaped array which can maintain a reasonable accuracy of localization is seven in the simulation case. The experimental results have also demonstrated that the L-shaped array is capable of providing satisfactory localization of a leak hole on a flat plate.

Though this research aimed to detect leaks from plate structures, the proposed technique is potentially applicable to cylindrical and spherical structures, which will be studied in the near future. Additionally, array topology is very complex if the number of sensors, the spacing between them and the layout are varied unevenly. For instance, further studies are required by varying the angle between the two segments of the L-shaped and cross arrays and the angles in the triangle and star arrays.

References

[1] Y. Yan, Y. Shen, X. Cui, Y. Hu, Localization of multiple leak sources using acoustic emission sensors based on MUSIC algorithm and wavelet Packet Analysis, IEEE SENS. J. 18 (2018) 9812-9820.

[2] P. S. Murvay, I. Silea, A survey on gas leak detection and localization techniques, J. LOSS PREVENT. PROC. 25 (2012) 966-973.

[3] S. Huang, W. Lin, M. Tsai, M. Chen, Fiber optic in-line distributed sensor for detection and localization of the pipeline leaks, SENSOR. ACTUAT. A-PHYS. 135 (2007) 570-579.

[4] G. Ye, K. Xu, W. Wu, Standard deviation based acoustic emission signal analysis for detecting valve internal leakage, SENSOR. ACTUAT. A-PHYS. 283 (2018) 340-347.

[5] S. Ravula, S. Narasimman, L. Wang, A. Ukil, Experimental Validation of Leak and Water-Ingression Detection in Low-Pressure Gas Pipeline Using Pressure and Flow Measurements, IEEE SENS. J. 17 (2017) 6734-6742.

[6] A. Mostafapour, S. Davoudi, Analysis of leakage in high pressure pipe using acoustic emission method, APPL. ACOUST. 74 (2013) 335-342.

[7] Y. Gao, M. Brennan, Y. Liu, F. Almeida, and P. Joseph, Improving the shape of the cross-correlation function for leak detection in a plastic water distribution pipe using acoustic signals, APPL. ACOUST. 127 (2017) 24-33.

[8] X. Wang, M. S. Ghidaoui, Identification of multiple leaks in pipeline II: Iterative

beamforming and leak number estimation, MECH. SYST. SIGNAL. PR., 119 (2019) 346-362.
[9] J. Wang, R. Zhang, Y. Yan, X. Dong, J. Li, Locating hazardous gas leaks in the atmosphere via modified genetic, MCMC and particle swarm optimization algorithms, ATMOS. ENVIRON. 157 (2017) 27-37.
[10] X. Han, S. Zhao, X. Cui, Y. Yan, Localization of CO2 gas leakages through acoustic emission multi-sensor fusion based on wavelet-RBFN modeling, MEAS. SCI. TECHNOL. 30 (2019) 085007.
[11] A. Ebrahimkhanlou, B. Dubuc, S. Salamone, A generalizable deep learning framework for localizing and characterizing acoustic emission sources in riveted metallic panels, Mech. Syst. Signal Process. 130 (2019) 248-272.
[12] A. Ebrahimkhanlou, S. Salamone, Single-Sensor Acoustic Emission Source Localization in Plate-Like Structures Using Deep Learning, Aerospace. 5 (2018) 50.
[13] F. Almeida, M. Brennan, P. Joseph, Y. Gao, A. Paschoalini, The effects of resonances on time delay estimation for water leak detection in plastic pipes, J. SOUND. VIB. 420 (2018) 315-329.
[14] P. Wilcox, M. Lowe, P. Cawley, The effect of dispersion on long-range inspection using ultrasonic guided waves, NDT&E INT. 34 (2001) 1-9.
[15] A. Ebrahimkhanlou, S. Salamone, Acoustic emission source localization in thin metallic plates: A single-sensor approach based on multimodal edge reflections, Ultrasonics. 78 (2017) 134–145.
[16] A. Ebrahimkhanlou, S. Salamone, A probabilistic framework for single-sensor acoustic emission source localization in thin metallic plates, Smart Mater. Struct. 26 (2017) 095026.
[17] X. Cui, Y. Yan, Y. Ma, L. Ma, X. Han, Localization of CO_2 leakage from transportation pipelines through low frequency acoustic emission detection, SENSOR. ACTUAT. A-PHYS. 237 (2016) 107-118.
[18] J. Kober, Z. Prevorovsky, M. Chlada, In situ calibration of acoustic emission transducers by time reversal method, SENSOR. ACTUAT. A-PHYS, 240 (2016) 50-56.
[19] M. Ferrante, B. Brunone, S. Meniconi, B. W. Karney, C. Massari, Leak size, detectability and test conditions in pressurized pipe systems, WATER RESOUR. MANAG. 28 (2014) 4583-4598.
[20] S. A. Jafar, A. Goldsmith, Transmitter optimization and optimality of beamforming for multiple antenna systems, IEEE T. WIREL. COMMUN. 3 (2004) 1165-1175.
[21] Y. Yan, X. Cui, M. Guo, X. Han, Localization of a continuous CO_2 leak from an isotropic flat-surface structure using acoustic emission detection and near-field beamforming techniques, MEAS. SCI. TECHNOL. 27 (2016) 115105.
[22] X. Bian, Y. Zhang, Y. Li, X. Gong, S. Jin, A new method of using sensor arrays for gas leakage location based on correlation of the time-space domain of continuous ultrasound, SENSORS 15 (2015) 8266-8283.
[23] X. Cui, Y. Yan, M. Guo, X. Han, Y. Hu, Localization of CO2 leakage from a circular hole on a flat-surface structure using a circular acoustic emission sensor array, SENSORS 16 (2016) 1951.
[24] E. D. Niri, S. Salamone, A probabilistic framework for acoustic emission source localization in plate-like structures, SMART MATER. STRUCT. 21 (2012) 1-16.
[25] T. He, Q. Pan, Y. Liu, X. Liu, D. Hu, Near-field beamforming analysis for acoustic emission source localization, Ultrasonics 52 (2012) 587-592.
[26] A. Mostafapour, S. Davoodi, M. Ghareaghaji, Acoustic emission source location in plates using wavelet analysis and cross time frequency spectrum, Ultrasonics 54 (2014) 2055-2062.